Interplay of structure and superconductivity in α-SnS tuned by pressure

Xindeng Lv [1], Simin Li [1], Yanping Huang,[1,*] and Tian Cui [1,2,†]

[1]*Institute of High Pressure Physics, School of Physical Science and Technology, Ningbo University, Ningbo 315211, China*

[2]*State Key Laboratory of Superhard Materials, College of Physics, Jilin University, Changchun 130012, China*

(Received 1 March 2024; revised 21 May 2024; accepted 1 August 2024; published 15 August 2024)

The emergent structure under high pressure introduces a distinctive lattice arrangement, deviating from conventional configurations and offering a unique landscape for exploring intriguing properties, especially in the domain of superconductivity. Here, we have systematically investigated the structural evolution and electrical properties of α-SnS under high pressure. The x-ray diffraction results indicate that SnS undergoes two phase transitions at 16.8 and 49.7 GPa, representing a second-order *Pnma* to *Cmcm* transition and a first-order *Cmcm* to $Pm\bar{3}m$ transition. In addition, single-crystal *in situ* high-pressure Raman spectroscopy experiments have confirmed it. Electrical transport measurements demonstrate the transition of SnS from a semiconductor to a metal and then to a superconductor under high pressure, intricately linked to a structural transition and an increase in the hole carrier concentration. Combined with our first principles calculation, it is determined that the topological properties and superconductivity coexist in SnS with the $Pm\bar{3}m$ phase. The nonmonotonic variation of T_c in SnS with pressure is attributed to the electron-phonon coupling effect. Additionally, this study marks a confirmation of the structural phase transitions in SnS under high pressure. Our study contributes to a deeper understanding of the intricate relationship between structure and performance in extreme conditions.

DOI: 10.1103/PhysRevB.110.054107

I. INTRODUCTION

Binary tin sulfide compounds have garnered extensive applications in optoelectronic devices owing to their distinctive structure, semiconductor properties, and remarkable electronic characteristics in recent years [1–6]. These compounds exhibit diverse configurations [7], such as orthorhombic *Pnma* [6], *Cmcm* [8] structures, and cubic $P2_13$ [9], $I\bar{4}3d$ [10] structures. The diverse structural landscape of binary tin sulfides manifests a broad spectrum of performances. Specifically, the *Pnma* phase in SnX (X = S, Se) showcases high thermoelectric efficiency and elevated optical absorption coefficients. Simultaneously, the $P2_13$ phase exhibits outstanding photovoltaic properties. Moreover, the presence of superconductivity has been observed in binary tin sulfides under high pressure, such as SnSe [11], Sn_3Se_4 [10], SnS [12], and Sn_3S_4 [13]. Therein, SnSe undergoes a complex structural phase transition from *Pnma* → *Cmcm* → $Pm\bar{3}m$, leading to its transformation from a semiconductor to a metal and ultimately exhibiting superconducting behavior under high pressure [11]. This intricate interplay between structure and properties underscores the versatility and potential applications of these materials in various electronic and optoelectronic devices.

SnS is an important member of binary tin sulfide compounds, which possess many excellent electronic and optoelectronic properties [14]. At ambient pressure, the *Pnma* phase of SnS exhibits semiconductor behavior with a direct optical band gap of 1.4 eV, and its optical absorption reaches a remarkable range 10^4–10^5 cm^{-1} [15]. Furthermore, SnS also possesses a high intrinsic carrier mobility [16]. Pressure, as a fundamental state parameter, plays a pivotal role in efficiently modulating the electronic structure and crystal lattice of materials [17–19]. In the initial high-pressure experiments, it was observed that the *Pnma* phase of SnS undergoes a first-order structural phase transition, changing from orthorhombic to monoclinic symmetry at 18 GPa [20]. Subsequent theoretical investigations suggested a transition from *Pnma* to *Cmcm* [21]. The $Pm\bar{3}m$ phase was subsequently postulated as the second new phase of SnS under high pressure, accompanied by superconducting transitions [12]. However, the current absence of direct x-ray diffraction (XRD) evidence poses challenges in conclusively establishing the existence of these high-pressure phases in SnS.

In this work, we performed a systematic high-pressure study of α-SnS by *in situ* x-ray diffraction, temperature-dependent electrical transport measurements, and first principles calculation. The results of the XRD experiments reveal two distinct structural phase transitions. The first phase transition occurs between 13 and 16.8 GPa, transforming from the *Pnma* to the *Cmcm* phase. Simultaneously, as evidenced by temperature-dependent electrical transport measurements, SnS undergoes a gradual transition into a metallic state, reaching metallization at 27.8 GPa. The second structural phase transition occurs at 49.7 GPa, which was associated with the superconductivity transition. This study offers a distinctive perspective on the intricate relationship between the structural evolution and properties of binary sulfur-containing tin compounds.

II. EXPERIMENTAL AND CALCULATION METHODS

α-SnS powders (purity 99.5%) were purchased from Alfa Aesar and α-SnS single crystals (purity 99.999%) were purchased from SUNANO New Energy Co. (Jiangsu, China).

*Contact author: huangyanping@nbu.edu.cn

†Contact author: cuitian@nbu.edu.cn

The α-SnS powders are characterized by XRD conducted on the D8 Advance to determine its crystal structure. The high-pressure synchrotron XRD was performed at the BL15U1, Shanghai Synchrotron Radiation Facility (SSRF), at room temperature without pressure transition medium (PTM). The diffraction patterns were refined by the Reflex modules in Material Studio and the Crystallography Data Analysis Software II (GSAS-II) [22,23]. High pressure Raman spectroscopy measurements were performed on a MonoVista CRS+ 500 Microscopic Confocal Raman System with a 532-nm laser and silicon oil was used as the PTM. Standard-four-point probe electrical transport measurements were carried out using a nonmagnetic diamond-anvil cell (DAC) made of Be-Cu alloy with 200-μm culets. We carried out two run resistance measurements with powder and single crystal samples, respectively. Powder sample #1 does not utilize PTM to ensure optimal contact conditions. Under the testing conditions of an applied magnetic field, the magnetic field direction is parallel to the α-axis direction and perpendicular to the direction of the current. For single crystal samples #2, NaCl was used as the PTM. Resistance and Hall resistance were measured simultaneously in this round of experiments. The $R1$ fluorescence line of ruby was used to determine pressures [24].

Our first-principles calculations were performed using the projector augmented waves method (PAW) [25] based on density functional theory (DFT) as implemented in the Vienna *ab initio* simulation package [26]. We used the Perdew-Burke-Ernzerhof (PBE) generalized gradient approximation (GGA) to describe the exchange-correlation density function. The cutoff energy was set to 600 eV, and the Brillouin zone was sampled using the Monkhorst-Pack k-point meshes with a resolution of $2\pi \times 0.03$ Å^{-1}. The forces on each atom were relaxed to less than 1.0×10^{-3} eV/Å. A finite displacement method was employed for phonon dispersion calculations with the PHONOPY method [27]. Superconducting properties were calculated in the framework of density-functional and the plane-wave pseudopotential method, as implemented in the QUANTUM ESPRESSO (QE) package [28].

III. RESULTS AND DISCUSSION

At ambient pressure, the bulk α-SnS belongs to a GeS-type structure, characterized by an orthorhombic system with the space group *Pnma*. The powder XRD pattern of α-SnS aligns well with the *Pnma* structure, as depicted in Supplemental Material Fig. S1(a) [29], with lattice parameters $a = 11.19$ Å, $b = 3.98$ Å, and $c = 4.33$ Å, which are in accordance with previous findings [3,30]. Figure S1(b) shows the structure of α-SnS [29], which is composed of stacked bilayer planes. Within each layer, Sn and S atoms alternate, forming a zigzag pattern along the b and c axes. The layers are bound together through a weak van der Waals interaction along the a axis. Figure S2 [29] shows the band structure of α-SnS at ambient pressure, revealing its semiconductor nature with a band gap of 0.95 eV.

Previous works on the structural transition in SnS were primarily focused on the theoretical aspects; there have been few *in situ* high-pressure experiments conducted to study the high-pressure structure of SnS. Therefore, to obtain the structural evolution of α-SnS under high pressure, *in situ* high-pressure XRD was conducted up to 68.1 GPa at room temperature ($\lambda = 0.6199$ Å) as shown in Fig. 1(a). At 0.8 GPa, all peaks can be indexed by orthorhombic structure with a *Pnma* space group [Fig. S3(a)] [29]. At 16.8 GPa, a noteworthy phenomenon is observed, where the two peaks at 10–12° exhibit a gradual merge into a single peak, which is associated with the phase transition. The previous theoretical works reported that SnS with the *Pnma* space group undergoes a structural phase transition to the β phase with the *Cmcm* space group under high pressure [21,30]. Furthermore, a comparable outcome has been observed in the sister compound SnSe [11]. At 42.2 GPa, the fitted results of Rietveld refinement as shown in Fig. S3(b) [29] illustrates the structure transformation from *Pnma* to *Cmcm*. Upon further compression, three new diffraction peaks emerge at $2\theta \approx 11.3°$, 16°, and 19.9°, as indicated by the arrows in Fig. 1(a), which suggests the second structure transition in SnS at 49.7 GPa. With a continuous pressure increase, the new peak becomes more robust up to 68.1 GPa. These three new peaks can be effectively indexed to the cubic structure of the $Pm\bar{3}m$ space group, coexisting with the *Cmcm* phase up to the maximum pressure of 68.1 GPa in this experiment [Fig. 1(e)]. This experimental observation of phase transition pathway in SnS under high pressure is despite earlier theoretical reports [21,31]. Lattice parameters evolved as a function of pressure were extracted in Fig. 1(c). The a axis and b axis are the interlayer directions of *Pnma* and *Cmcm*, respectively, and therefore they are more easily compressed than the other axes due to the interlayer van der Waals interaction. Figure 1(b) displays the pressure dependence of the volume indicating a second-order phase transition from *Pnma* to *Cmcm*, while the transition from *Cmcm* to $Pm\bar{3}m$ is a first-order phase transition accompanied by a 7.7% volume collapse that fitted by the third-order Birch-Murnaghan equation of state [32]:

$$P = \frac{3}{2}B_0\left[\left(\frac{V_0}{V}\right)^{7/3} - \left(\frac{V_0}{V}\right)^{5/3}\right] \times \left\{1 + \frac{3}{4}(B_0' - 4)\left[\left(\frac{V_0}{V}\right)^{2/3} - 1\right]\right\},$$

and yields $V_0/Z = 50$ Å^3, $B_0 = 28.4$ GPa, and $B' = 9.4$ with *Pnma* SnS, $V_0/Z = 45.1$ Å^3, $B_0 = 95.2$ GPa with *Cmcm* SnS, and $V_0/Z = 37.7$ Å^3 and $B_0 = 175.6$ GPa with $Pm\bar{3}m$ SnS and for *Cmcm* and $Pm\bar{3}m$ phase, given $B' = 4$. The increase in bulk modulus under high pressure indicates that the material becomes progressively resistant to compression at elevated pressures.

The phases of *Pnma* and *Cmcm* exhibit a typical layered structure, and the distinction between the *Pnma* phase and the *Cmcm* phase lies in the one Sn atom bonds with three and five S atoms, respectively. The detailed crystallographic data are shown in Table S1 [29]. However, the $Pm\bar{3}m$ exhibits a CsCl-type phase and an Sn atom coordinate with the eight nearest S atoms. Therefore, the significant structural differences result in a substantial volume collapse during the structural phase transition from *Cmcm* to $Pm\bar{3}m$ (Fig. S4) [29]. To validate the dynamic stability of *Cmcm* and $Pm\bar{3}m$ under high pressure, we conducted phonon dispersion calculation, as illustrated in Fig. 1(d) and Fig. S5 [29]. All phonon frequencies were found

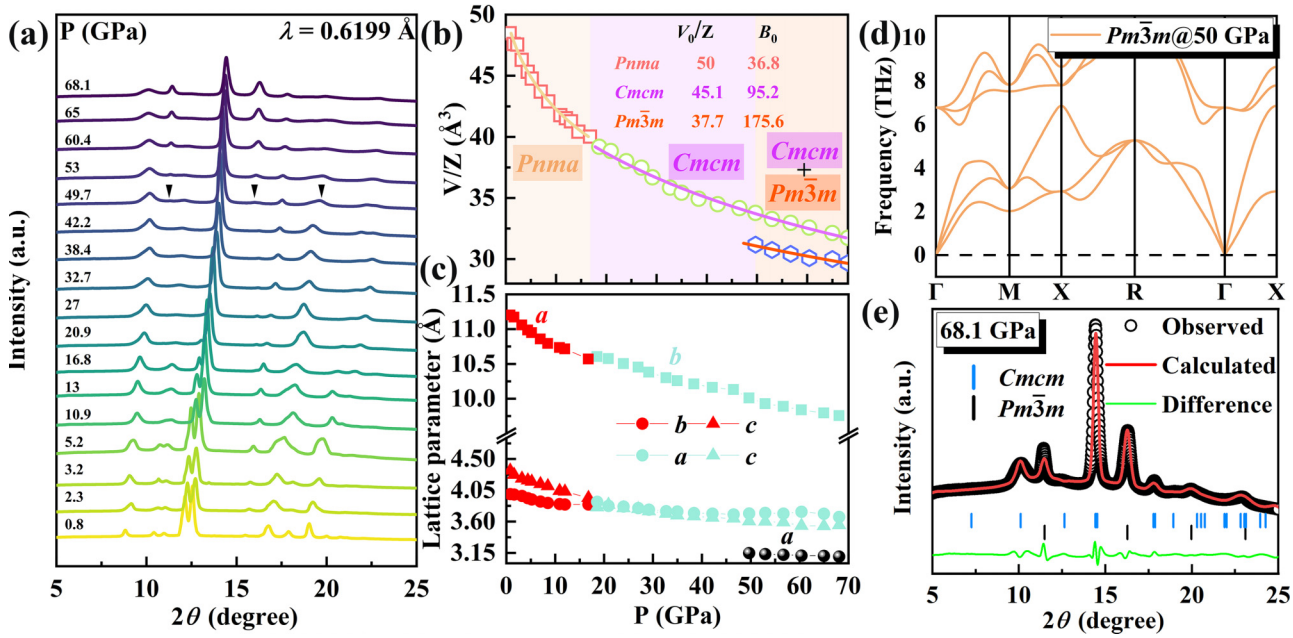

FIG. 1. (a) The collected XRD patterns of SnS under various pressures. The black arrows indicate three new peaks. (b) Lattice parameter dependence of pressure for three phases. (c) The volume dependence of pressure and the line represent the fit results of the third-order Birch-Murnaghan equation of state. (d) Calculated phonon dispersions for $Pm\bar{3}m$-SnS at 50 GPa. (e) Full-profile Rietveld refinements of XRD patterns at 68.1 GPa.

to be nonimaginary, indicating the dynamic stability of *Cmcm* and $Pm\bar{3}m$, respectively.

To further understand the structural evolution of SnS under high pressure, we performed Raman spectroscopy measurements of single-crystal samples under quasihydrostatic pressure conditions. Figure 2 shows the results of the Raman spectra on single-crystal sample SnS from 0.4–51 GPa. At ambient pressure, the α-SnS crystal structure has 21 optical

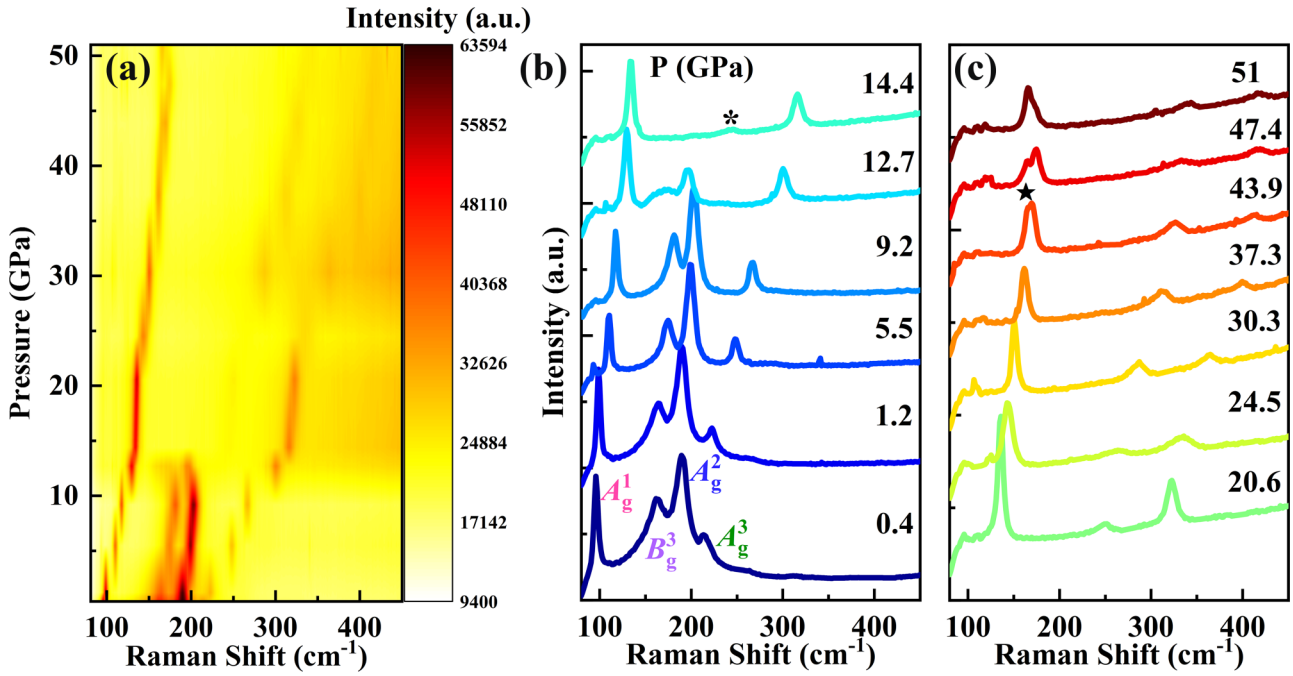

FIG. 2. Vibrational properties of single-crystal SnS under various pressures measured at room temperature. (a) Two-dimensional contour plots on the evolution of vibrational modes at high pressures up to 51 GPa. Raman spectra of SnS for different pressures range with (b) 0.4–14.4 and (c) 20.6–51 GPa at room temperature. The asterisks mark additional peaks that occur during the first and second structural transitions at 14.4 and 43.9 GPa, respectively.

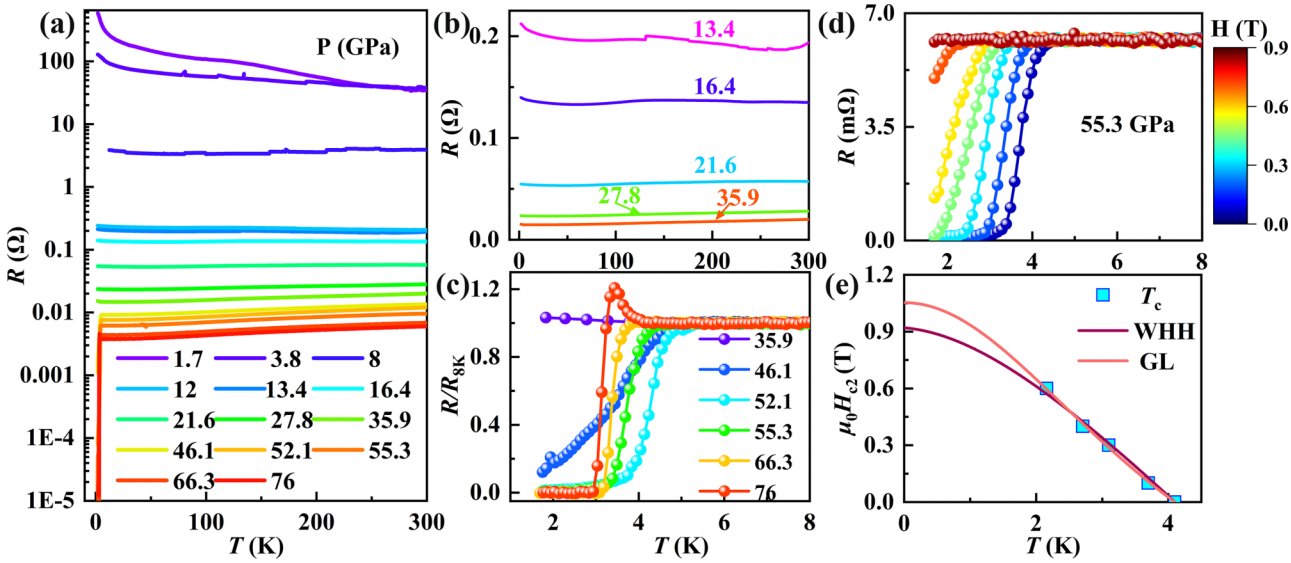

FIG. 3. Resistance as a function of temperature under high pressure in powder sample α-SnS. (a) Temperature-dependent resistance under various pressures from 1.7–76 GPa in log scale. (b) Electrical resistance as a function of temperature at 13.4–35.9 GPa. (c) Enlarged the low-temperature region at 35.9–76 GPa. (d) Variation of sample resistance with applied magnetic field at 55.3 GPa. (e) The $\mu_0 H_{c2}$ plots at various temperatures around T_c.

modes. Using the irreducible representation,

$$\Gamma = 4A_g + 2A_u + 4B_{1g} + B_{1u} + 2B_{2g} + 3B_{2u} + 2B_{3g} + 3B_{3u},$$

12 of these modes are Raman active, including $4A_g$, $2B_{1g}$, $4B_{2g}$ modes and $2B_{3g}$ modes. At 0.4 GPa, we detected four Raman-active modes of α-SnS, namely $A_g^1 = 95.9\ \mathrm{cm}^{-1}$, $A_g^2 = 189.4\ \mathrm{cm}^{-1}$, $A_g^3 = 213.3\ \mathrm{cm}^{-1}$, and $B_{3g} = 162.8\ \mathrm{cm}^{-1}$, which are in excellent agreement with the previous study [9,33]. The remaining Raman-active vibrational modes were not detected, either due to their low frequency or low intensity. With increasing pressure, all Raman modes exhibit a blueshift (shift to higher frequencies). However, the B_{3g} and A_g^2 modes become undetectable above 12.7 GPa. Importantly, a new Raman peak emerges at 14.4 GPa at around 245 cm^{-1} [Fig. 2(b)], indicating a second-order phase transition in the SnS crystal, which is in agreement with our synchrotron XRD results. The new Raman peak represents the bonding of neighboring Sn and S atoms (Fig. S4) [29]. Additionally, the Raman frequency shift shows that the slope of the A_g^3 mode changes significantly after 14.4 GPa, suggesting enhanced interlayer coupling in the SnS structure (Fig. S6). Upon further compression, the A_g^1 mode exhibits splitting at 43.9 GPa; the positions of the new peaks are obtained through Gaussian fitting (Fig. S7) [29], representing the structural transformation *Cmcm* to $Pm\bar{3}m$ phase. However, there is no Raman activity in the $Pm\bar{3}m$ phase. Therefore, the emergence of the new peak may be attributed to the formation of lattice defects, such as vacancies, interstitial atoms, or dislocations, during the phase transition from *Cmcm* to $Pm\bar{3}m$. In summary, the Raman results are consistent with our synchrotron XRD results, demonstrating that SnS can undergo a phase transition from *Pnma* to *Cmcm* to $Pm\bar{3}m$ under nonhydrostatic pressure conditions.

To investigate the electronic properties of α-SnS under high pressure, we conducted electrical transport measurements at various pressures, and the results are presented in Figs. 3(a)–3(e). At 1.7 GPa, the resistance increases with temperature, displaying a typical semiconductor behavior. With the pressure increased, the resistance gradually decreased in the whole temperature range. A semiconductor-metal transition can be observed at 16.4 GPa. But at the low-temperature region, the electronic character performance of a semiconductor has a distinctive combination of metallic and semiconductor behavior, indicating a structural phase transition from *Pnma* to *Cmcm* combined with our XRD results. Furthermore, at 21.6 GPa, the $R(T)$ curve exhibits a negative dR/dT at temperatures exceeding 50 K. However, the persistence of resistance divergence at low temperatures suggests the influence of grain boundary scattering in the powder sample [30,34,35]. Additionally, the resistance upturn at low temperatures gradually diminishes with increasing pressure (Fig. S8) [29]. Intriguingly, at 46.1 GPa, following the complete suppression of the upturn in low-temperature resistance, a notable phenomenon emerges—a sudden drop in resistance at around 4.4 K, and this observation has been corroborated by previous studies, confirming its origin as the superconducting transition [12]. However, the discrepancies in the T_c may be attributed to variations between powder and single-crystal samples. Combining our XRD studies, it can be inferred that the origin of superconducting transitions in SnS under high pressure is associated with structural phase transitions. Upon further compression, zero resistance is observed at 52.1 GPa, with the maximum T_c reaching 4.6 K. It is notable to mention that the zero-resistance state was not observed in previous studies, and our study further confirms the superconductivity of SnS under high pressures. With further compression, the T_c shifts to lower temperatures, which reaches 3.3 K at 76 GPa. It is noticeable that at 76 GPa an upturning behavior of resistance could be observed in the low-temperature region; a hump in resistance has been extensively documented in prior studies of disordered systems

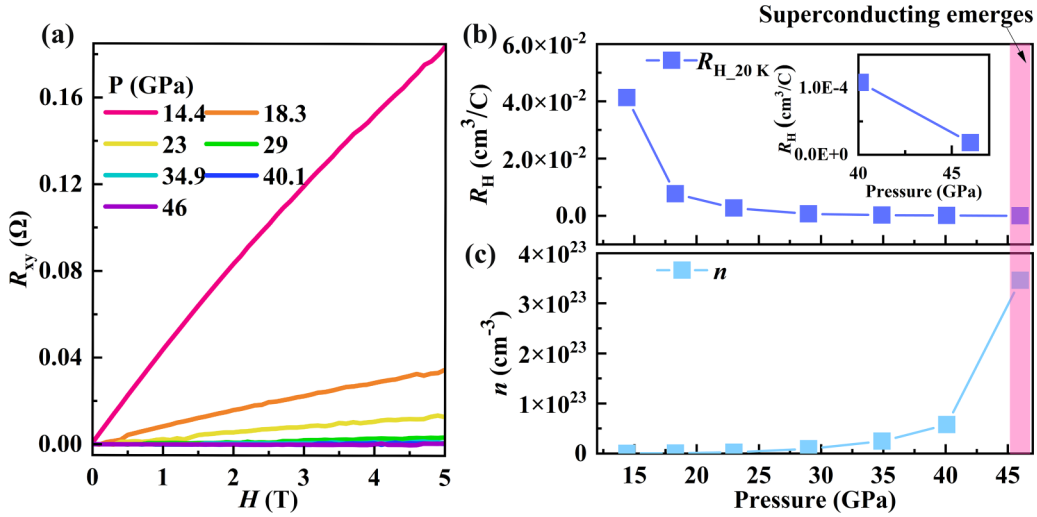

FIG. 4. (a) Pressure dependence of Hall resistance curves $R_{xy}(H)$ of α-SnS single crystal at 20 K. (b) Hall coefficient at 20 K variation with pressure. The inset shows enlarged data for Hall coefficients in the range 40–46 GPa. (c) Carrier concentration n as a function of pressure.

[36–38]. To further confirm the superconducting transition, the resistance dependence of various magnetic fields is examined, the drop of resistance was gradually suppressed with the magnetic field applied at 55.3 GPa [Fig. 3(d)], and the upper critical fields (μH_{c2}) are estimated to be 0.9 and 1.05 T using the Ginzburg-Landau function [39] and Werthamer-Helfand-Hohenberg (WHH) equation [40], respectively [Fig. 3(e)]. This is similar to the previous results [12].

To further investigate the origin of superconductivity in pressurized SnS, we carried out high-pressure Hall effect measurements accompanied by resistance measurements using single crystal samples. Figure S9 [29] shows the temperature-dependent resistance results of run2, and it can be seen that the resistance measurements of the single crystals are almost identical to the powder samples, demonstrating the high reproducibility of this experiment (Fig. 3). Figure 4(a) shows the Hall $R_{xy}(H)$ curves measured at 20 K with the magnetic field (H) ranging -5 to $+5$ T under different pressures. At 14.4 GPa, the slope of the Hall resistance is positive, implying that the carrier type is dominated by hole-type carriers which is consistent with the previous study [12,30], and the slope decreases gradually with further compression indicating a gradual increase in the carrier concentration. In order to clearly observe the change of carrier concentration with pressure, we extracted the Hall coefficient and carried out the calculation of the carrier concentration by single band Drude model $n = -1/(eR_H)$, and the results are shown in Figs. 4(b) and 4(c). In the pressure range 14.4 to 40 GPa, the carrier concentration increases gradually; moreover, at 46 GPa, the carrier concentration increases sharply. Thus, the appearance of superconductivity is accompanied by a structural transition and an increase in the hole carrier concentration.

In the BCS theory, the origin of superconductivity is linked to electron-phonon interactions. The Debye temperature characterizes the nature of lattice vibrations, which is crucial for the interaction between electrons and phonons. The relationship between the T_c and the Debye temperature can be approximated as follows:

$$T_c \propto \frac{\theta_D}{e^{\frac{1}{N(0)V}}},$$

where θ_D is the Debye temperature, $N(0)$ is the electronic density of states (density of electronic states at the Fermi surface), and V is the effective coupling constant for electron-phonon interactions. Therefore, we use the Bloch-Grinensen equation [41],

$$R(T) = R_0 + A\left(\frac{T}{\theta_D}\right)\int_0^{\theta_D/T}\frac{x^5}{(e^x-1)(1-e^{-x})}dx,$$

to fit the $R(T)$ curves and calculate the θ_D, where the parameters A, θ_D, and R_0 were determined through the application of the least square method (Fig. S10, Table S2) [29]. As illustrated in Figs. 5(a) and 5(b), the variations of θ_D and T_c as functions of pressure demonstrate a robust and consistent correlation. In addition, we obtained consistent results in a second round of multichannel experiments (Figs. S11 and S12) [29]. In general, modulation of the Debye temperature impacts raising the T_c, as it reflects the phonon energy distribution in the material, directly related to electron-phonon interactions. To provide further confirmation regarding the origin of the superconducting transition, we conducted calculations of the projected phonon density of states (PHDOS), the Eliashberg spectral function $\alpha^2F(\omega)$, and the electron-phonon coupling (EPC) at 60 GPa for the $Pm\bar{3}m$ phase. From the PHDOS in Fig. 5(c), the frequency spectrum below 7 THz is predominantly attributed to vibrations originating from the Sn atoms, while for frequencies above 7 THz, the spectrum is largely dominated by the S atoms. The calculated λ and the logarithmic average phonon frequency ω_{log} is 0.5 and 327.3 K, respectively. To estimate the T_c at 60 GPa, we use the Allen-Dynes modified McMillan formula with Coulomb pseudopotential $\mu^* = 0.1$. The obtained T_c is approximately 4 K, which aligns well with our electrical transport measurements. Therefore, we have demonstrated

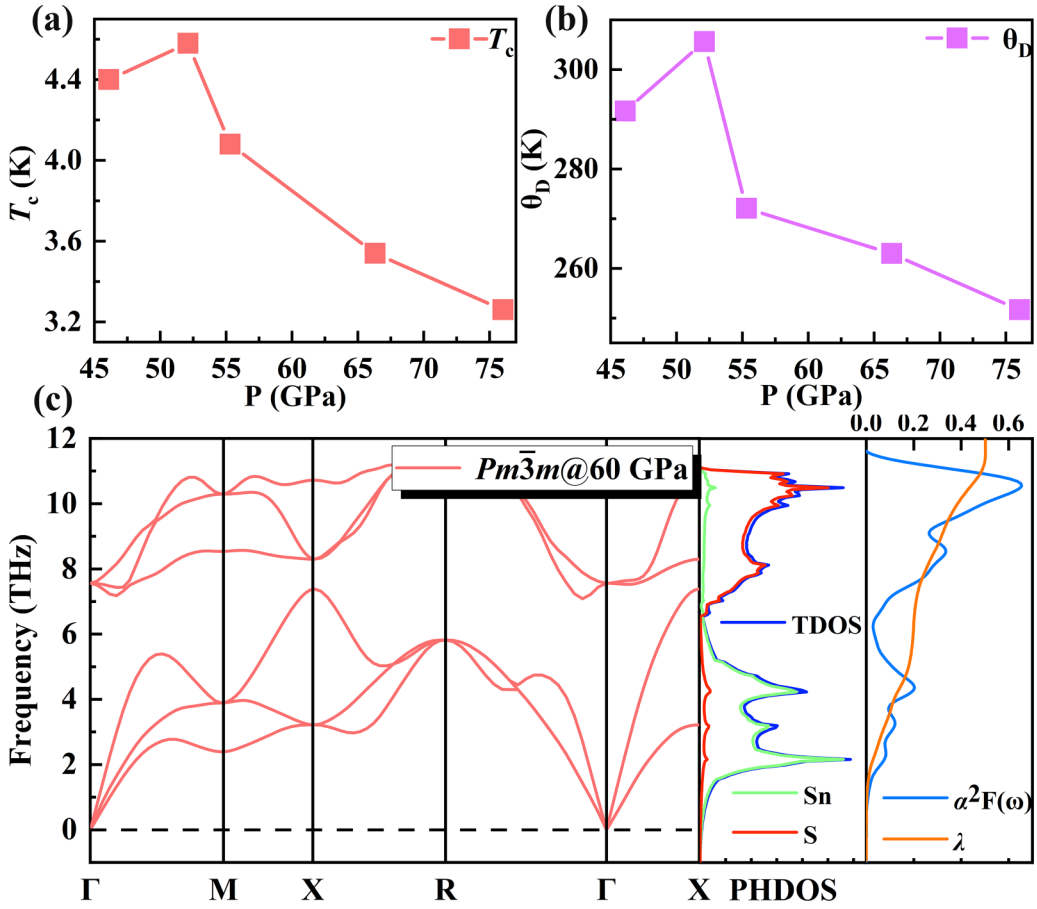

FIG. 5. Variation of the (a) superconducting transition temperature and (b) Debye temperature with pressure. (c) Calculated the phonon dispersions, phonon density of states (PHDOS), the Eliashberg spectral function $\alpha^2F(\omega)$, and the electron-phonon integral $\lambda(\omega)$ for $Pm\bar{3}m$ phase.

that the superconducting phase in SnS originates from the $Pm\bar{3}m$ phase.

To further investigate the electronic structures of SnS with the CsCl structure under pressure, we calculated the band structure and DOS at 50 GPa. The results are presented in Fig. 6. As shown in Figs. 6(a) and 6(c), the band structures of SnS with the CsCl structure exhibit typical metallic behavior, consistent with observations from electronic transport experiments. The density of states at the Fermi level is mainly contributed by the Sn-*p* and S-*p* orbitals [Fig. 6(b)]. Interestingly, without considering the spin-orbit coupling, the bands along the *M*-*X*, and *X*-*R* paths cross, near the Fermi level. The results imply that the SnS with CsCl structure exhibits topological properties without considering SOC. This parallels the behavior observed in its sister compound, SnSe, under high pressure [11]. Furthermore, Liu *et al.* reported the presence

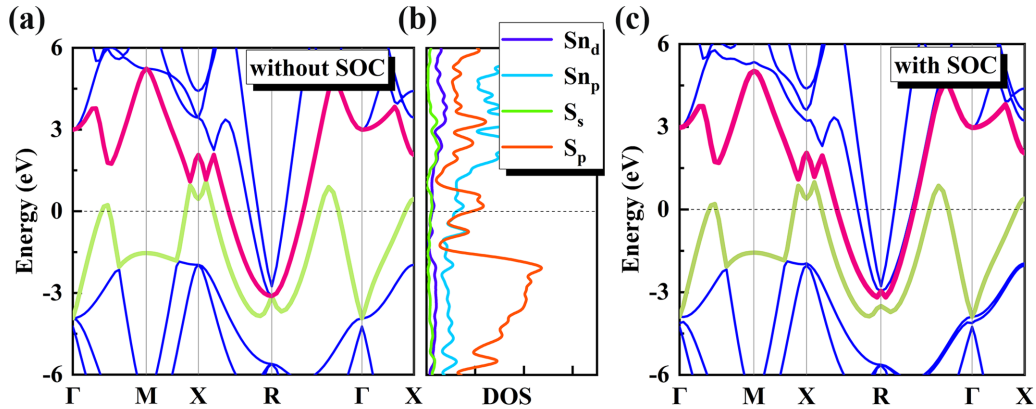

FIG. 6. The band structure and DOS of SnS with the CsCl structure under 50 GPa. (a) The calculated band structures of SnS without SOC. (b) Projected density of states (DOS) of SnS without SOC. (c) The calculated band structures of SnS with SOC.

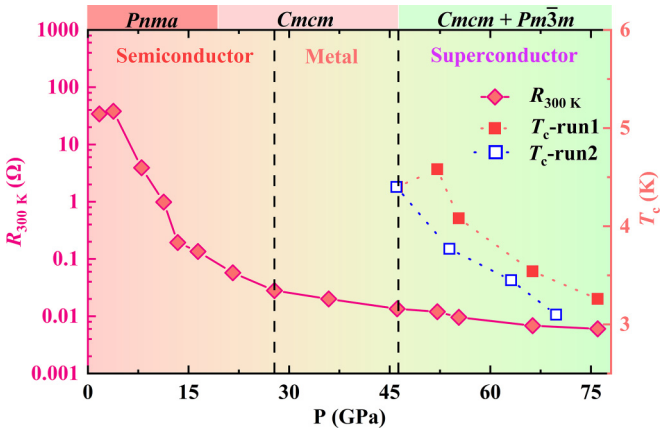

FIG. 7. Phase diagram of SnS from temperature-dependent electrical transport and XRD measurement.

of topological properties in the InSe with CsCl structure. These findings suggest a broader trend within compounds with CsCl-type structures, indicating a potential connection between the structural motif and the emergence of topological characteristics [42].

Based on the results of the experiment, we have mapped out a phase diagram, as shown in Fig. 7. In the low-pressure region, the resistance at 300 K decreases by three orders of magnitude until reaching 27.8 GPa. Beyond 27.8 GPa, the change in electrical resistance at 300 K gradually becomes less pronounced, indicating a transition from a semiconductor to a metallic state. Subsequently, a superconducting transition occurs at 46.1 GPa, accompanied by a structural phase transition from *Cmcm* to $Pm\bar{3}m$. Notably, T_c undergoes a complex behavior, which exhibits a slight increase with pressure, reaching its maximum at 52.1 GPa, and followed by a subsequent decline from 52.1 to 76 GPa. These results provide robust evidence for structural transition, metallization, and superconductivity transition in SnS under high pressure.

IV. CONCLUSION

In summary, our study examines the structural evolution and electrical properties of SnS under high pressure using *in situ* XRD, electrical transport measurements, Raman spectrum measurements, and first-principles calculations. We identify two phase transitions at 16.8 and 49.7 GPa: a second-order *Pnma* to *Cmcm* transition and a first-order *Cmcm* to $Pm\bar{3}m$ transition. Electrical transport measurements reveal the semiconductor-to-metal-to-superconductor transition under high pressure, closely tied to the structural phase transitions, and moreover, a structural transition and an increase in the hole carrier concentration. The variation in T_c is attributed to electron-phonon coupling. Our calculations show that topological properties and superconductivity coexist in SnS with the $Pm\bar{3}m$ phase. This study contributes to a deeper understanding of the intricate relationship between structure and performance at extreme conditions.

ACKNOWLEDGMENTS

The authors thank the staff of the BL15U1 beamline of the Shanghai Synchrotron Radiation Facility (SSRF). This work was supported by National Key R&D Program of China (Grant No. 2022YFA1405500), National Natural Science Foundation of China (Grants No. 52072188 and No. 12304072), Program for Science and Technology Innovation Team in Zhejiang (Grant No. 2021R01004), and Natural Science Foundation of Ningbo (Grant No. 2021J121). This work was also supported by the User Experiment Assist System of the Shanghai Synchrotron Radiation Facility (SSRF).

[1] L.-D. Zhao, S.-H. Lo, Y. Zhang, H. Sun, G. Tan, C. Uher, C. Wolverton, V. P. Dravid, and M. G. Kanatzidis, Ultralow thermal conductivity and high thermoelectric figure of merit in SnSe crystals, Nature (London) **508**, 373 (2014).

[2] M. Parenteau and C. Carlone, Influence of temperature and pressure on the electronic transitions in SnS and SnSe semiconductors, Phys. Rev. B **41**, 5227 (1990).

[3] M. Guc, J. Andrade-Arvizu, I. Y. Ahmet, F. Oliva, M. Placidi, X. Alcobé, E. Saucedo, A. Pérez-Rodríguez, A. L. Johnson, and V. Izquierdo-Roca, Structural and vibrational properties of α- and π-SnS polymorphs for photovoltaic applications, Acta Mater. **183**, 1 (2020).

[4] F. Li, H. Wang, R. Huang, W. Chen, and H. Zhang, Recent advances in SnSe nanostructures beyond thermoelectricity, Adv. Funct. Mater. **32**, 2200516 (2022).

[5] X. Zhou, Q. Zhang, L. Gan, H. Li, J. Xiong, and T. Zhai, Booming development of group IV–VI semiconductors: Fresh blood of 2D family, Adv. Sci. **3**, 1600177 (2016).

[6] L. A. Burton and A. Walsh, Phase stability of the earth-abundant tin sulfides SnS, SnS_2, and Sn_2S_3, J. Phys. Chem. C **116**, 24262 (2012).

[7] I. Pallikara and J. M. Skelton, Phase stability of the tin monochalcogenides SnS and SnSe: A quasi-harmonic lattice-dynamics study, Phys. Chem. Chem. Phys. **23**, 19219 (2021).

[8] H. Fridman, N. Barsheshet, S. Kolusheva, T. Mokari, S. Hayun, and Y. Golan, Real-time monitoring of phase transitions in π-SnS nanoparticles, Nanoscale **15**, 8881 (2023).

[9] R. E. Abutbul, E. Segev, L. Zeiri, V. Ezersky, G. Makov, and Y. Golan, Synthesis and properties of nanocrystalline π-SnS – a new cubic phase of tin sulphide, RSC Adv. **6**, 5848 (2016).

[10] H. Yu, W. Lao, L. Wang, K. Li, and Y. Chen, Pressure-stabilized tin selenide phase with an unexpected stoichiometry and a predicted superconducting state at low temperatures, Phys. Rev. Lett. **118**, 137002 (2017).

[11] X. Chen, P. Lu, X. Wang, Y. Zhou, C. An, Y. Zhou, C. Xian, H. Gao, Z. Guo, C. Park, B. Hou *et al.*, Topological Dirac line nodes and superconductivity coexist in SnSe at high pressure, Phys. Rev. B **96**, 165123 (2017).

[12] R. Matsumoto, P. Song, S. Adachi, Y. Saito, H. Hara, A. Yamashita, K. Nakamura, S. Yamamoto, H. Tanaka, T. Irifune *et al.*, Pressure-induced superconductivity in tin sulfide, Phys. Rev. B **99**, 184502 (2019).

[13] R. Matsumoto, K. Terashima, S. Nakano, K. Nakamura, S. Yamamoto, T. D. Yamamoto, T. Ishikawa, S. Adachi, Tetsuo Irifune, M. Imai *et al.*, High-pressure synthesis of superconducting Sn_3S_4 using diamond anvil cell with boron-doped diamond heater, Inorg. Chem. **61**, 10 (2022).

[14] W. Shi, M. Gao, J. Wei, J. Gao, C. Fan, E. Ashalley, H. Li, and Z. Wang, Tin selenide (SnSe): Growth, properties, and applications, Adv. Sci. **5**, 1700602 (2018).

[15] K. T. Ramakrishna Reddy, N. Koteswara Reddy, and R. W. Miles, Photovoltaic properties of SnS based solar cells, Sol. Energ. Mat. Sol. C **90**, 3041 (2006).

[16] R. E. Banai, L. A. Burton, S. G. Choi, F. Hofherr, T. Sorgenfrei, A. Walsh, B. To, A. Cröll, and J. R. S. Brownson, Ellipsometric characterization and density-functional theory analysis of anisotropic optical properties of single-crystal α -SnS, J. Appl. Phys **116**, 013511 (2014).

[17] J. Feng, C. Li, W. Deng, B. Lin, W. Liu, R. Susilo, H. Dong, Z. Chen, N. Zhou, X. Yi *et al.*, Superconductivity induced by Lifshitz transition in pristine SnS_2 under high pressure, J. Phys. Chem. Lett. **13**, 9404 (2022).

[18] S. Lee, Y. T. Lee, S. G. Park, K. H. Lee, S. W. Kim, D. K. Hwang, and K. Lee, Dimensional crossover transport induced by substitutional atomic doping in $SnSe_2$, Adv. Electron. Mater. **4**, 1700563 (2018).

[19] N. V. Morozova, I. V. Korobeynikov, N. Miyajima, and S. V. Ovsyannikov, Giant room-temperature power factor in *p*-Type thermoelectric SnSe under high pressure, Adv. Sci. **9**, 2103720 (2022).

[20] L. Ehm, K. Knorr, P. Dera, A. Krimmel, P. Bouvier, and M. Mezouar, Pressure-induced structural phase transition in the IV–VI semiconductor SnS, J. Phys.: Condens. Matter **16**, 3545 (2004).

[21] S. Alptekin and M. Durandurdu, Formation of a *Cmcm* phase in SnS at high pressure; an *ab initio* constant pressure study, Solid State Commun. **150**, 870 (2010).

[22] B. H. Toby and R. B. Von Dreele, *GSAS-II:* The genesis of a modern open-source all purpose crystallography software package, J. Appl. Crystallogr. **46**, 544 (2013).

[23] H. M. Rietveld, A profile refinement method for nuclear and magnetic structures, J. Appl. Crystallogr **2**, 65 (1969).

[24] H. K. Mao, J. Xu, and P. M. Bell, Calibration of the ruby pressure gauge to 800 Kbar under quasi-hydrostatic conditions, J. Geophys. Res. **91**, 4673 (1986).

[25] P. E. Blochl, Projector augmented-wave method, Phys. Rev. B **50**, 17953 (1994).

[26] G. Kresse and J. Furthmüller, Efficiency of ab-initio total energy calculations for metals and semiconductors using a plane-wave basis set, Comput. Mater. Sci. **6**, 15 (1996).

[27] A. Togo and I. Tanaka, First principles phonon calculations in materials science, Scr. Mater. **108**, 1 (2015).

[28] P. Giannozzi, S. Baroni, N. Bonini, M. Calandra, R. Car, C. Cavazzoni, D. Ceresoli, G. Chiarotti, M. Cococcioni, I. Dabo *et al.*, QUANTUM ESPRESSO: A modular and open-source software project for quantum simulations of materials, J. Phys.: Condens. Matter **21**, 395502 (2009).

[29] See Supplemental Material at http://link.aps.org/supplemental/10.1103/PhysRevB.110.054107 for Rietveld refinement result of α-SnS at different pressures, pressure dependence of Raman mode, and calculations of phonon and band structure of SnS.

[30] F. Ke, J. Yang, C. Liu, Q. Wang, Y. Li, J. Zhang, L. Wu, X. Zhang, Y. Han, B. Wu, Y. Ma, and C. Gao, High-pressure electrical-transport properties of SnS: Experimental and theoretical approaches, J. Phys. Chem. C **117**, 6033 (2013).

[31] J. M. Gonzalez, K. Nguyen-Cong, B. A. Steele, and I. I. Oleynik, Novel phases and superconductivity of tin sulfide compounds, J. Chem. Phys **148**, 194701 (2018).

[32] F. Birch, Finite elastic strain of cubic crystals, Phys. Rev. **71**, 809 (1947).

[33] J. M. Skelton, L. A. Burton, A. J. Jackson, F. Oba, S. C. Parker, and A. Walsh, Lattice dynamics of the tin sulphides SnS_2, SnS, and Sn_2S_3: Vibrational spectra and thermal transport, Phys. Chem. Chem. Phys. **19**, 12452 (2017).

[34] X. Ming, Y. Zhang, X. Zhu, Q. Li, C. He, Y. Liu, T. Huang, G. Liu, B. Zheng, H. Yang, J. Sun, X. Xi, and H. Wen, Absence of near-ambient superconductivity in $LuH_{2\pm x}N_y$, Nature (London) **620**, 72 (2023).

[35] C. R. M. Grovenor, Grain boundaries in semiconductors, J. Phys. C: Solid State Phys. **18**, 21 (1985).

[36] L. Ma, K. Wang, Y. Xie, X. Yang, Y. Wang, M. Zhou, H. Liu, X. Yu, Y. Zhao, H. Wang, G. Liu, and Y. Ma, High-temperature superconducting phase in clathrate calcium hydride CaH_6 up to 215 K at a pressure of 172 GPa, Phys. Rev. Lett. **128**, 167001 (2022).

[37] L. Kang, Z.-Y. Cao, and B. Wang, Pressure-induced electronic topological transition and superconductivity in topological insulator $Bi_2Te_{2.1}Se_{0.9}$, J. Phys. Chem. Lett. **13**, 11521 (2022).

[38] H. Yamamoto, M. Ikeda, and M. Tanaka, Giant resistivity anomaly in A15 Nb_3 (Ge, Si) superconductive films with compositionally modulated superstructure, Jpn. J. Appl. Phys. **24**, L314 (1985).

[39] V. L. Ginzburg and L. D. Landau, On the theory of superconductivity, in *On Superconductivity and Superfluidity: A Scientific Autobiography* (Springer, Berlin, 2009), pp. 113–137.

[40] N. R. Werthamer, E. Helfand, and P. C. Hohenberg, Temperature and purity dependence of the superconducting critical field, H_{c2}. III. Electron spin and spin-orbit effects, Phys. Rev. **147**, 295 (1966).

[41] J. M. Ziman, *Electrons and Phonons: The Theory of Transport Phenomena in Solids* (Oxford University Press, Oxford, 2001).

[42] S. Liu, Y. Yang, F. Yu, X. Wen, Z. Gui, K. Peng, R. Wang, and J. Ying, Pressure-induced superconductivity and nontrivial band topology in compressed γ-InSe, Phys. Rev. B **105**, 214506 (2022).